Universiteit Leiden
The Netherlands

Mid-infrared spectroscopy of starbursts : from Spitzer-IRS to JWST-MIRI

Martínez-Galarza, J.F.

Citation

Martínez-Galarza, J. F. (2012, June 19). *Mid-infrared spectroscopy of starbursts : from Spitzer-IRS to JWST-MIRI*. Retrieved from https://hdl.handle.net/1887/19113

Version:	Corrected Publisher's Version
License:	Licence agreement concerning inclusion of doctoral thesis in the Institutional Repository of the University of Leiden
Downloaded from:	https://hdl.handle.net/1887/19113

Note: To cite this publication please use the final published version (if applicable).

Cover Page

Universiteit Leiden

Leiden University Repository

The handle http://hdl.handle.net/1887/19113 holds various files of this Leiden University dissertation.

Author: Martínez-Galarza, Juan Rafael
Title: Mid-infrared spectroscopy of starbursts : from Spitzer-IRS to JWST-MIRI
Date: 2012-06-19

CHAPTER 3

Ongoing massive star formation in NGC 604[1]

NGC 604 is the second most massive H II region in the Local Group, thus an important laboratory for massive star formation. Using a combination of observational and analytical tools that include *Spitzer* spectroscopy, *Herschel* photometry, *Chandra* imaging and Bayesian Spectral Energy Distribution (SED) fitting, we investigate the physical conditions in NGC 604, and quantify the amount of massive star formation currently taking place. We derive an average age of 4 ± 1 Myr and a total stellar mass of $1.6^{+1.6}_{-1.0} \times 10^5$ $M_\odot$ for the entire region, in agreement with previous optical studies. Across the region we find that the X-ray field destroys small aromatic molecules and excites the emission of [Si II]. Within NGC 604 we identify several individual bright infrared sources with diameters of about 15 pc and luminosity weighted masses between 10^3 $M_\odot$ and 10^4 $M_\odot$. Their spectral properties indicate that some of these sources are embedded clusters in process of formation, which together account for ~8% of the total stellar mass in the NGC 604 system. The variations of the radiation field strength across NGC 604 are consistent with a sequential star formation scenario, with at least two bursts in the last few million years. Our results indicate that, while NGC 604 is a more evolved H II region as compared to its largest sibling 30 Doradus, star formation in NGC 604 is still ongoing, triggered by the earlier bursts.

[1]Based on: J.R. Martínez-Galarza, D. Hunter, B. Groves and B. Brandl, 2012, Submitted to ApJ

3.1 Introduction

Despite their importance in the structure and evolution of galactic systems, via strong radiative and mechanical input into the surrounding interstellar medium (ISM), our understanding of massive star formation regions remains poor, both on observational and theoretical grounds. From an observational point of view, a number of reasons make the study of massive star formation a challenging topic in astrophysics, as pointed out in the comprehensive review on the issue by Zinnecker & Yorke (2007). Regions of massive star formation are highly embedded in thick layers of dust during the crucial early stages of their existence. In addition, these early stages are short-lived, leaving little time for the study of their evolution. Another problem is the lack of spatial resolution in the observations. Most of extragalactic giant star forming regions are often contained within a single pixel. Finally, most massive stars form in close proximity to each other, and their mutual influence via gravitational interaction, powerful outflows, supernova events and strong winds contributes to the complexity of the problem.

Observations of nearby star forming regions provide an excellent laboratory for the study of a particular aspect of this interaction, namely the triggering of new star formation events by gas compression resulting either from a ionization shock front created by the radiation field of a previous generation of stars, or by the supersonic shocks of a supernova event. In the classical theory by Elmegreen & Lada (1977), an ionization front compresses an adjacent layer of molecular gas and heats it, producing a gravitational instability that will eventually result in a new generation of stars. In order to test this and other theories of triggered star formation, it is important to unequivocally determine and quantify the amount of currently ongoing star formation in Giant H II Regions (GH IIRs), and its relation to the ionizing radiation from previous generations of stars.

After 30 Doradus, NGC 604 is the second most massive GH IIR in the Local Group. Located in the Traingle Galaxy (M33) at a distance of 0.84 Mpc (Freedman et al. 1991), it harbors several associations of massive stars distributed across an area of about 200 pc on the side, dominated by a cluster containing $\sim$ 200 OB stars (Hunter et al. 1996). These associations have excavated a complex system of filaments and cavities of ionized material surrounded by photon-dominated regions (PDRs) and molecular gas (see, for example Relaño & Kennicutt 2009,for a discussion on the spatial distribution of emission in the region). Optical studies reveal an age of the region between 3 and 5 Myr (Hunter et al. 1996, González Delgado & Pérez 2000) and a total stellar mass of $(3.8 \pm 0.6) \times 10^5 \mathrm{M}_\odot$. Individual CO molecular clouds have been detected with sizes between 5 and 29 pc and with masses of between 0.8×10^5 $\mathrm{M}_\odot$ and 7.4×10^5 $\mathrm{M}_\odot$ (Miura et al. 2010). Relaño & Kennicutt (2009) have carried out a photometric multi-wavelength study of NGC 604 and derived an average extinction in the line of sight towards NGC 604 of $A_V = 0.30$ and a stellar mass of about $(5.7 \pm 0.4) \times 10^5 \mathrm{M}_\odot$ for the region, not too far from the mass estimate of Eldridge & Relaño (2011).

Several attempts have been made to quantify the total amount of ongoing massive star formation in NGC 604. Using near-infrared (NIR) observations with the *Hubble Space Telescope* (HST), Barbá et al. (2009) identify several sources that coincide spatially with radio-peak structures, and argue that this is suggestive of their star-forming nature. More

recently, Fariña et al. (2012) report the discovery of sources with near infrared excess within the infrared-bright ridges surrounding the ionized gas, and associate them with Massive Young Stellar Objects (MYSO). Relaño & Kennicutt (2009) argue that the reddening observed towards some prominent sources in the region can be explained by the existence of foreground molecular material, but they do not rule out the possibility of those sources being embedded sites of star formation. The use of infrared spectrophotometry combined with physical modeling provides a powerful tool to distinguish between foreground extinction and embedded star formation, which complements the photometric methods that use near-infrared colors as discriminators between the two cases, and could be.

In this chapter we perform a comprehensive analysis of the physical conditions in NGC 604 in the context of its evolutionary status, and investigate the presence of ongoing massive star formation in the region. We use infrared spectral and photometric data from the *Spitzer* and *Herschel* Space Telescopes, complemented with archival X-ray and optical data, as well as a set of analytical tools to interpret them. We report the discovery of individual infrared knots whose derived masses are consistent with them being stellar cluster in process of formation. This is also supported by Bayesian fitting of the Spectral Energy Distribution (SED) of the region, which points to the presence of a significant component of embedded objects in the region. We derive line emission and continuum maps of NGC 604 and use them to assess the variations in radiation field strength, ionization levels and extinction across the GH II R, and find that our results are consistent with a sequential star formation history in the last $\sim$ 4 Myr. We also discuss some additional findings regarding the role of X-ray emission in the enhancement of both [Si II] atomic emission and 17 μm PAH emission.

The chapter is structured as follows. In §3.2 we present the IRS data and describe the data reduction to obtain the maps and the spatially integrated spectrum of NGC 604. §3.3 describes the resulting maps and spectra, as well as the tools used to extract physical information from the observations. In §3.4 we discuss the results of our analysis in terms of the current evolutionary stage of NGC 604 and the presence of ongoing star formation in the region. We conclude with a summary of our main results in §3.5.

3.2 Data reduction and ancillary datasets

Most of our analysis will be based on *Spitzer* Infrared Spectrograph (IRS) (Houck et al. 2004) data of a region encompassing the bulk of infrared emission from NGC 604. However, to provide more robust constraints on the physics of the region, we also use complementary photometry from the *Spitzer* Infrared Array Camera (IRAC) (Fazio et al. 2004) and from the *Herschel Space Observatory* Photodetector Array Camera and Spectrometer (PACS) (Poglitsch et al. 2010). Additionally, we use archival *Hubble Space Telescope-Wide Field and Planetary Camera 2* and *Chandra X-ray Observatory-ACIS* images.

3.2.1 IRS data

The *Spitzer* Infrared Spectrograph (IRS) provides unprecedented spatial resolution and sensitivity as compared to any previous mid-IR spectroscopic observations of the NGC 604 region. The spectral resolving power ranges from $R \sim 60$ at short wavelengths to $R \sim 120$ at the long-wavelength edge. The sensitivity is about 100 times better than that of the spectrometer onboard the *Infrared Space Observatory* (ISO), while the spatial resolution is a factor of 10 larger. The wavelength coverage of the IRS ranges from about 5 μm to about 38 μm.

IRS observations of the NGC 604 region were obtained in January 2006 using the IRS mapping mode for spectroscopy, which consists of the acquisition of slit spectra using a grid of positions around a central target. These observations were part of the program *Comparative Study of Galactic and Extragalactic H* II *Regions* (P. I. J. Houck). Only the low resolution modules short-low (SL1, SL2) and long-low (LL1, LL2) of the IRS were used for this set of observations. For the SL modules, 12 slit pointings were made with each of the two spectrometer orders covering an area on the sky of about $55'' \times 40''$, which corresponds to a physical scale of about 225 pc $\times$ 160pc at the distance of NGC 604 (see Fig. 3.1). The slice width for the SL modules is $3''.6$, corresponding to a pixel scale of $1''.85\,\mathrm{px}^{-1}$ ($7.5\,\mathrm{pc\,px}^{-1}$). For the LL modules, the slice width is $10''.5$, which corresponds to a pixel scale of $5''.08$ px^{-1} (20.5 pc px^{-1}) and 6 pointings were made with each order to cover an area of about 720 pc $\times$ 205 pc.

In addition to the spectral map with the IRS low resolution modules (lores data hereafter), we also use IRS staring mode observations of three specific locations within the region using the high resolution modules of the spectrometer (hires data here after). For these modules the wavelength coverage is shorter (between $9.9 and 38.0\,\mu$m), but the resolving power is significantly higher ($R \approx 600$). The locations of the staring mode observations are within the area of the spectral map and correspond approximately to the positions of the peaks of 8 μm emission, associated with PAH emission, as discussed later. The high resolution slits are wider than their low resolution counterparts ($4''.7$ and $11''.1$ for the short-high and long-high orders respectively) and therefore their spectral apertures are also larger than the spatial resolution elements of the spectral maps.

Extraction of the spectra

For the staring mode data, the Spitzer Science Center Tool IRSCLEAN was used to remove cosmic rays and then SMART v.8.0 was used with the full aperture mode for extended sources, based on the size of the slits compared to the source NGC 604, which is large enough to be considered extended. The observation cycles were co-added and the sky background removed using an additional off-source background exposure taken as part of the campaign. We have applied a scaling factor to the fluxes extracted in the long-hig (LH) module to match the overlap region in the short-high (SH) module. This is an aperture correction to account for the larger size of the LH slit with respect to the SH slit. The scaling factors for the LH spectra towards fields A, B an C are 0.28, 0.41 and 0.41 respectively (see Fig. 3.2).

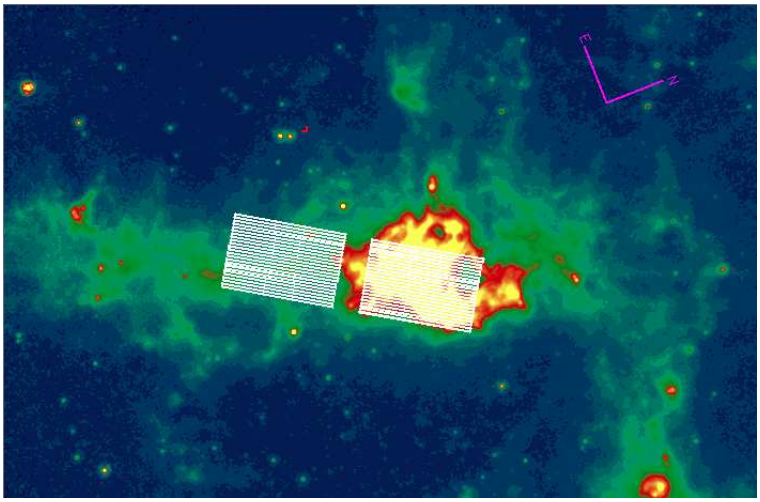

Figure 3.1 The target and background slit pointings superimposed on the IRAC 8 μm image of NGC 604. The green structure near the H II region is part of the spiral arm structure of M33. See text for a discussion on the flux levels.

For the spectral map, we extracted the spatially integrated spectrum of the region for all four IRS orders using a extraction aperture corresponding to the SL coverage of the map (see Fig. 3.2), which includes the bulk of the IR emission of NGC 604. Some of the extended filamentary structure of the region, which is one order of magnitude dimmer than the peaks of emission, is left outside this area. The low surface brightness of these filaments and the bubble-like geometry that we will assume when modeling the region implies that this will be unimportant for the purposes of the present analysis. The background subtraction was performed using the order of the SL and LL modules that was not centered at the source during the corresponding exposure. The software package CUBISM (Smith et al. 2007) performs the data cube build-up once the background and the correct slit pointings have been provided. The background levels are not exactly the same for the low resolution and high resolution modules. The reason is that the orientation of opposite orders of the slit is different for different modules. In the case of the low resolution modules, the background picks up some emission from M33's spiral arm (See Fig. 3.1). This is our best estimate for the sky levels in the SL modules. For reference, the measured IRAC 8 μm flux levels on the spiral arm ($\sim$ 10 MJy sr^{-1}) are only 20% higher than the sky level outside the arm ($\sim$ 8 MJy sr^{-1}), and correspond to about 7% of the peak of 8 μm emission in the region.

Spectra can be extracted from each spatial pixel of the resulting data cube. The spatially integrated spectrum over the entire aperture is obtained by summing up the individual spectra of all resolution elements. We use the same extraction area for all modules and orders using the tools provided by CUBISM to make sure that the final spectrum for each order corresponds to the same physical region.

In addition to the spectrum of the integrated region, we have extracted the lores spectra of individual sources that we discuss in §3.3.1. For this extraction we use an aperture of a single SL pixel (1″.85). The CUBISM software allows us to extract the spectra in the LL spectral module with this small aperture, by scaling down the fluxes of the larger LL pixels to the SL sizes. This is equivalent to applying a scaling factor to match the different orders of IRS spectra, and introduces additional flux uncertainties in the long wavelength modules, where the PSF is not well sampled. Nonetheless, we consider this scaling a good approximation of the actual fluxes at smaller scales, since the SL pixels are not sufficiently small to resolve the sources, and the LL pixels are not large enough to include more than one source.

By selecting a single pixel aperture, we have chosen to loose some spatial information on the individual sources, because a single pixel samples only half of the PSF FWHM, and in exchange we avoid off-source flux contamination. More important than a full sampling of the PSF for our analysis, are the variations of the PSF with wavelength, that might introduce artifacts in the measured spectral features. Using calibration data, Pereira-Santaella et al. (2010) characterized the PSF variations with wavelength for the IRS reconstructed PSFs. Apart from an ondulating behavior of the PSF size with wavelength, that they attribute to alignment issues and to the reconstruction algorithm used, they compute variations of less that 10% on the PSF FWHM for the SL module. This is, as we will see in §3.2, below the observational errors in our data. The PSF of the LL module is affected by fringing and is difficult to characterize.

3.2.2 IRAC photometry

As part of the same Spitzer program, IRAC maps of the NGC 604 region were obtained with the camera filters with nominal wavelengths at 3.6 μm, 4.5 μm, 5.8 μm and 8 μm. The pixel scale for these maps is 1.2 arcsec px^{-1}, and they cover an area of about $5' \times 9'$, several times larger than the area covered by the spectral map. For the purpose of this chapter we have extracted the integrated flux of each map within a rectangular aperture area equal to the extraction area of the IRS spectral map. We perform this extraction using the FUNTOOLS package for the SAO *ds9* software. The sky background is estimated from the map by measuring the flux in a box of the same size as the map, but shifted to the west, to an area where no source emission is observed. In Table 3.1 we list the measured photometry. The listed uncertainties correspond to absolute flux calibration uncertainties ($\sim$ 3%), which are derived for point sources taking several systematic effects into account, as described in Reach et al. (2005).

The IRAC maps provide a sharper view of the region at specific wavelengths, and will allow the identification of interesting sources.

3.2.3 PACS photometry

Imaging maps of the host galaxy M33 have been obtained with the Herschel PACS instrument using the green (100 μm) and red (160 μm) filters as part of the HERM33ES

Wavelength [μm]	Flux [Jy]
3.6	0.067(0.002)
4.5	0.062(0.002)
5.8	0.322(0.010)
8.0	0.922(0.028)

Table 3.1 Integrated IRAC photometry of NGC 604.

Herschel key project (Kramer et al. 2010). The maps were obtained with a slow scan speed of 20 arcsec s^{-1}, and cover a total area of about $70' \times 70'$. Here we use the integrated photometry of an area of the PACS maps equivalent to the size of the IRS spectral maps (bottom panel of Fig. 3.2). The pixel sizes are $3''.2$ for the green band and $6''.4$ for the red band, or about 2 and 4 times the IRS-SL pixel size. The obtained fluxes, integrated over the entire area of the map, are $F_{100\mu\mathrm{m}} = 39.7 \pm 4.0$ Jy and $F_{160\mu\mathrm{m}} = 30.1 \pm 3.0$ Jy. The 10% uncertainty comes from a combination of absolute calibration errors, uncertainties associated with differences in the PSF at 100 μm and 160 μm and different pixel sizes in the two bands that lead to aperture uncertainties. The rms noise levels of the PACS maps are 2.6 mJy px^{-2} and 6.9 mJy px^{-2}.

3.2.4 HST-WFPC2 F555W data

We use the optical images obtained at 0.55 μm with the *Hubble* WFPC2 using the F555W filter, described in Hunter et al. (1996). At angular resolutions of $0''.1$, this optical map reveals the location of the massive ionizing clusters that provide the radiative input for the NGC 604 system.

3.2.5 Chandra X-ray Observatory-ACIS data

We use archival data from the *Advanced CCD Imaging Spectrometer* (ACIS) onboard the *Chandra X-ray Observatory*. The data were taken as part of the Chandra proposal "The Giant Extragalactic Star-Forming Region NGC 604" (Proposal ID 02600453, P.I. F.Damiani), and consist of a soft (0.5-1.2 keV) X-ray image of the entire nebula, with an exposures time of 90 ks. The pixel scale is $1''$ px^{-1}.

3.3 Analysis

We analyse the multi-wavelength observations described above using a set of analytical and statistical tools that are based on physical models of the region, and that we will describe shortly. The models compute the radiative transfer of the UV radiation as it traverses the ionized gas and molecular material around the H II region. They also compute

the dynamical evolution of its the expanding H II region. We use these tools to derive physical properties of the region, such as dust temperatures, total stellar mass, hardness of the radiation field and ionization state of the gas. In this section we present the obtained maps and spectra and describe the analytical tools that we use.

3.3.1 Distribution of the emission

Overall distribution

In Fig. 3.2(a) we show a three-color map of NGC 604 composed from the 3.6 μm and 8.0 μm IRAC channels together with the WFPC2 image at 0.55 μm. The blue channel shows the photospheric emission from young massive stars, most of which belong to the dense clustered structure labelled as "cluster A" by Hunter et al. (1996). Other, more spread stellar associations are seen next to the bright lobes of infrared emission. The 8 μm emission traces warm dust and the 7.7 μm PAH feature, and hence the location of the PDRs, while the 3.6μm traces a combination of the 3.3 μm PAH feature, very hot dust and photospheric emission from stellar populations older than 10 Myr. The filamentary and shell-like structure of the region observed at optical wavelengths is also visible in the mid-infrared.

Relaño & Kennicutt (2009) have shown that the 8 μm emission delineates the Hα shells in the boundaries between cavities. Most of the infrared emission in our maps comes from two lobes oriented in a SE-NW direction and that constitute the bulk of the emission at the IRAC bands. These lobes coincide with the edges of two main cavities observed in the region (cavities B1 and B2 in Tüllmann et al. (2008)), with diameters of approximately 50 pc each (see Fig. 3.2). They also coincide with the position of bright radio knots identified by Churchwell & Goss (1999). Within these cavities sits the majority of the luminous stars observed by HST (blue stellar sources in Fig. 3.2). An exhaustive X-ray study of the region carried out by Tüllmann et al. (2008) showed that the distribution of high energy photons inside these cavities is consistent with them being shaped by the mass loss and radiative pressure of about 200 OB stars. The eastern portion of NGC 604, on the other hand, seems to be an older part of the system, with X-ray emission consistent with a more evolved population.

The two lobes have similar surface brightness at 8 μm, but they show differences in their morphology. At the IRAC wavelengths, the SE lobe shows a series of subcondensations, some of which are notably brighter at 3.6 μm, while the NW lobe shows a more uniform distribution of emission. CO maps of the region reveal several molecular clouds in the region, with a CO-bright cloud peaking near the SE infrared lobe and extending southwards, and a dimmer and smaller cloud peaking near the NW lobe (Wilson & Scoville 1992). A number of MYSO candidates have been identified along these two lobes as sources with NIR excess (see, for example Fariña et al. 2012). By combining observational and SED modelling tools, in this chapter we will provide additional evidence that supports the star formation scenario, and quantifies its contribution to the total stellar mass in the region.

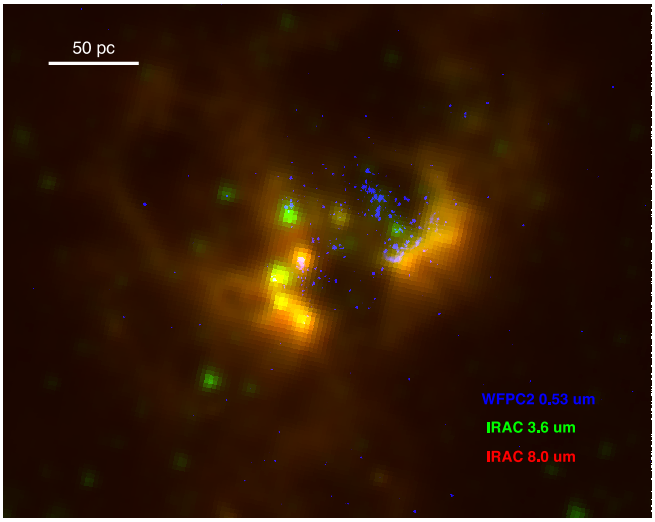

(a)

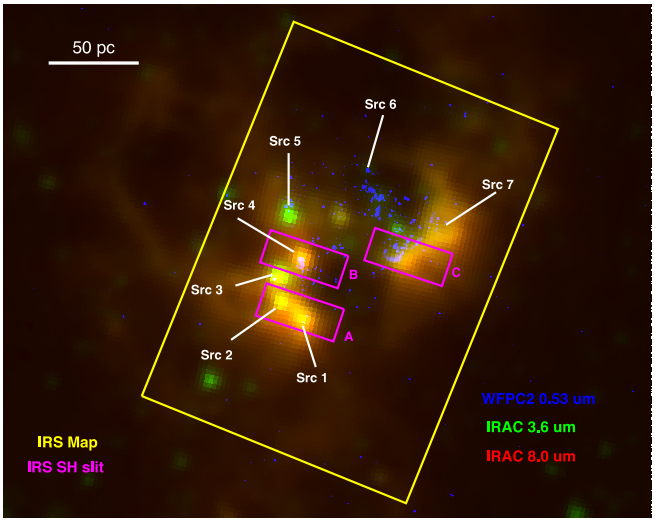

(b)

Figure 3.2 *(a)* Three-color Hubble/Spitzer map of NGC 604. The IRAC 8 μm band traces the PDR material, while the 3.6 μm band traces both PAH and photospheric emission from young stars. The WFPC2 image shows the location of the hot massive stars. *(b)* the same map with superimposed apertures of the IRS slits and labels for seven sources of interest based on their IRAC colors. We discuss these sources in the text and indicate their location in the map. The yellow rectangle corresponds to the extraction window for the IRS map and for the photometry, while the smaller magenta boxes show the location of the IRS SH slit for the high resolution observations. North is up, east is to the left.

Source	RA	Dec
Src 1	1h34m33.43s	+30°46′48.50″
Src 2	1h34m33.67s	+30°46′51.01″
Src 3	1h34m33.70s	+30°46′54.86″
Src 4	1h34m33.43s	+30°46′57.11″
Src 5	1h34m33.56s	+30°47′03.00″
Src 6	1h34m32.73s	+30°47′09.32″
Src 7	1h34m31.99s	+30°46′59.95″
A	1h34m33.6s	+30°46′51″
B	1h34m33.6s	+30°46′58″
C	1h34m32.4s	+30°46′59″

Table 3.2 Coordinates of the sources with extracted lores.

Individual sources.

In Fig. 3.2(b) we show again the three color map of with the superimposed extraction area for the lores spectral map and the location of the short-high IRS slits for the hires observations listed in Table 3.2. The extraction area for the spectral map includes the bulk of the emission in the IRAC bands and the stellar cluster. We have selected 7 individual sources of interest in the spectral map, including the well defined subcondensations that are visible in the IRAC images. These sources are indicated in Fig. 3.2(b), with their positions listed in Table 3.2. Sources A and B of the hires observations coincide with selected sources of the lores map. Specifically, source A includes sources 1 and 2, while source B includes source 4. Source C does not include any of the selected lores targets, but belongs to the NW infrared lobe, and is close to source 7. Also, sources A, B and C correspond to radio sources B, A and C, respectively, of Churchwell & Goss (1999), while source 6 is slightly shifted from the cluster A of Hunter et al. (1996).

We have fitted Gaussian profiles to the flux distribution of the observed subcondensations to investigate their spatial extension of the PAH emitting regions. Our fits reveal that they have projected diameters of about 3″.6 at 8 μm as measured from the FWHM of the Gaussian fits. The diffraction-limited resolution of the IRAC camera at this wavelength is 1″.71, and hence we conclude that the subcondensations are spatially resolved at 8 μm, having a diameter of at least two IRAC resolution elements. At the distance of NGC 604, their projected sizes correspond to physical diameters of about 15 pc, and hence they are comparable to the size of a typical giant molecular cloud.

Source	$F_{15\mu m}$ [MJy sr^{-1}]	$F_{30\mu m}$ [MJy sr^{-1}]	$F_{15\mu m}/F_{30\mu m}$
Src 1	102.8(10.3)	432.1(43.2)	0.238(0.034)
Src 2	65.4(6.5)	310.4(31.0)	0.211(0.030)
Src 3	95.8(9.6)	582.8(58.3)	0.164(0.023)
Src 4	95.9(9.6)	447.5(44.8)	0.214(0.030)
Src 5	25.8(2.6)	258.5(25.9)	0.100(0.014)
Src 6	10.1(1.0)	99.2(9.9)	0.101(0.014)
Src 7	113.5(11.4)	493.9(49.4)	0.230(0.033)
NGC 604	16.8(1.7)	100.93(10.1)	0.166(0.023)

Table 3.3 Continuum slopes of the SED for all seven sources and the region as a whole.

3.3.2 Infrared spectra

Extracted spectra

In Fig. 3.3 we show the IRS spectra of the integrated region and the selected sources of Table 3.2. The vertical axis is in units of flux density ($\nu F\nu$), and we have scaled them for the purpose of direct comparison. The integrated spectrum of NGC 604 has prominent PAH emission and some of the nebular lines detected are from species such as [Ar III], [Ne III], [Ne II], [S IV], [S III] and [Si II]. The thermal continuum increases monotonically in the IRS range.

Fig. 3.4 shows the high resolution spectra of the staring mode targets. The wavelength coverage of the hires modules is smaller than the lores case, from $\sim$ 10 μm to $\sim$ 37 μm, but the higher spectral resolving power allows the resolution of lines not seen in the lores spectra, such as the lines resulting from pure rotational transitions of molecular hydrogen, H_2 S(2) at 12.3 μm and H_2 S(1) at 17.0 μm. These lines are usually hard to detect on top of a strong continuum, due to the fact that they arise from quadrupolar rotational transitions, which are intrinsically weak.

Continuum emission

In order to characterize the spectral slope of the thermal continuum, we measure the flux densities at 15 μm and 30 μm using a range of wavelengths around the corresponding central wavelength containing about 20 resolution elements (14.75 μm -15.25 μm for the 15 μm measurement and 29.5 μm -30.5 μm for the 30 μm measurement), and we calculate the ratio $F_{15\mu m}/F_{30\mu m}$ for each source as well as the integrated spectrum. The spectral slopes give an indication of the dust temperature. Higher values of $F_{15\mu m}/F_{30\mu m}$ are associated with a hotter component of the dust, whereas lower values of this ratio indicate colder dust temperatures. We list the measured slopes in Table 3.3.

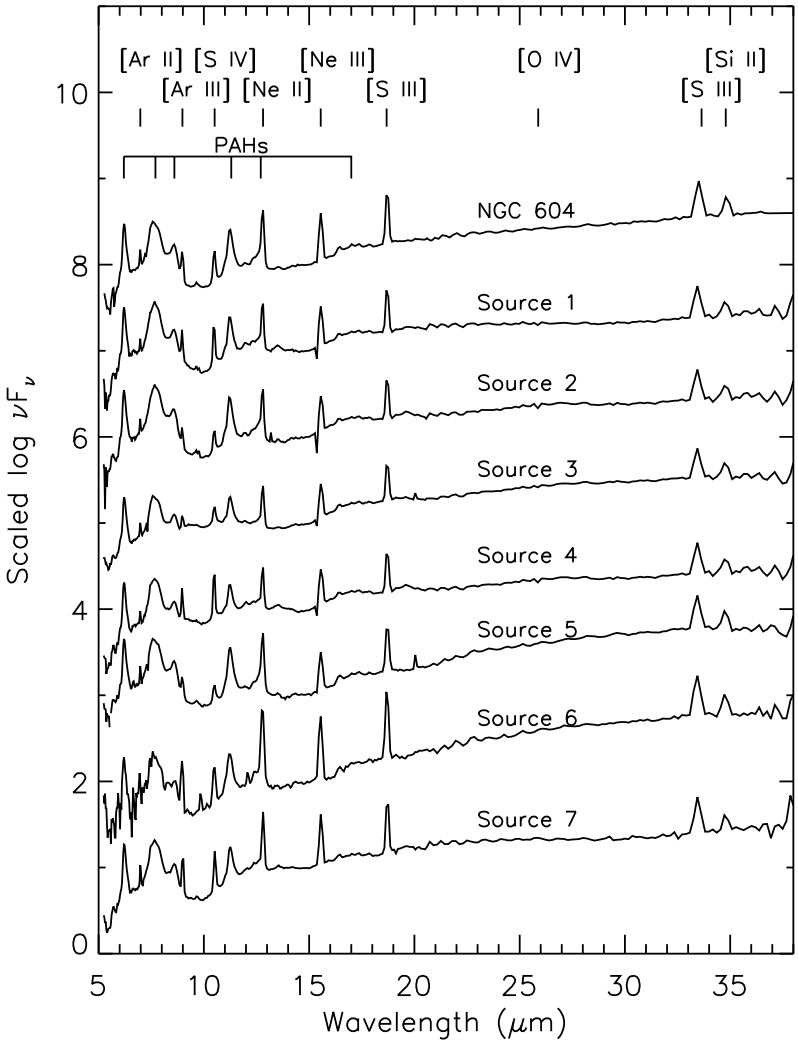

Figure 3.3 IRS spectra of the integrated NGC 604 region and the individual sources listed in Table 3.2. The position of some prominent mid-infrared fine structure lines are indicated, as well as the location of the PAH bands. The small feature seen at ~20 μm in sources 3 and 5 is an artifact from the data reduction.

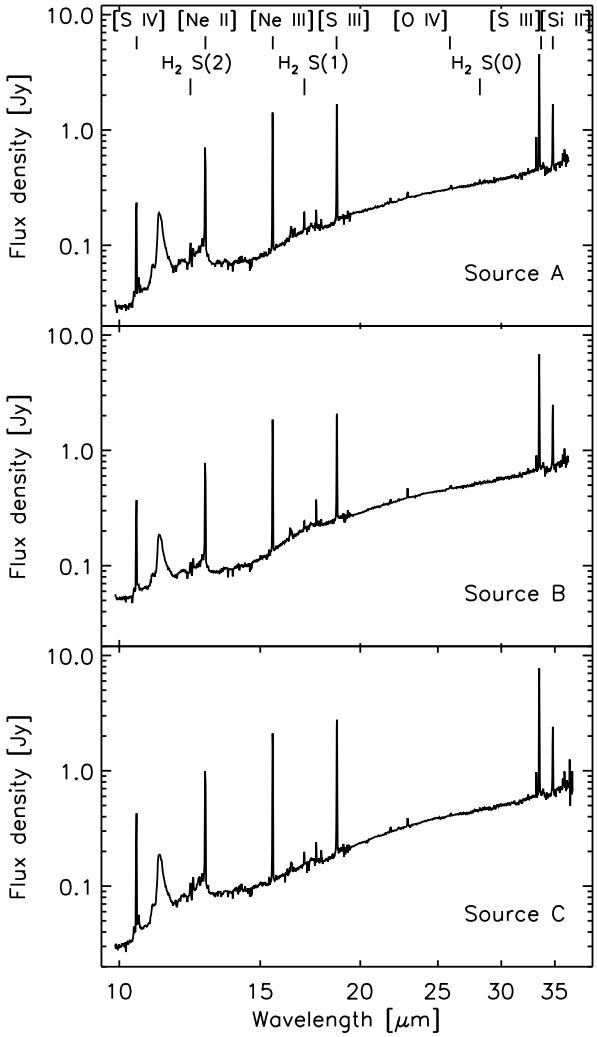

Figure 3.4 High resolution spectra of the three locations labeled A, B and C in Fig. 3.2. The prominent nebular and molecular hydrogen lines are indicated.

PAH emission

We have measured the strengths of the individual PAH features using the PAHFIT tool (Smith et al. 2007), which decomposes the IRS spectrum in individual contributions from dust thermal continuum, PAH features and fine-structure lines, as well as rotational lines of molecular hydrogen. In Table 3.4 we list the measured continuum-subtracted strengths of the different PAH components. The 7.7 μm strength was obtained by adding the PAHFIT 7.4 μm 7.6 μm and 7.8 μm features. Similar combinations of the 11.2 μm and 11.3 μm strengths for the 11.3 μm feature and the 16.4 μm, 17.0 μm, 17.4 μm and 17.9 μm for the 17 μm feature were performed.

In general, the ratios between PAH features remain constant for all sources. An interesting exception is the ratio of the $\mathrm{PAH}_{17\mu\mathrm{m}}$ feature to the sum of all other PAH features, ΣPAH (ΣPAH = $\mathrm{PAH}_{6.2\mu\mathrm{m}}$ + $\mathrm{PAH}_{7.7\mu\mathrm{m}}$ + $\mathrm{PAH}_{8.6\mu\mathrm{m}}$ + $\mathrm{PAH}_{11.3\mu\mathrm{m}}$). This ratio peaks strongly towards source 3, which is also a local peak of soft X-ray emission. In Table 3.5 we list the $\mathrm{PAH}_{17\mu\mathrm{m}}/\Sigma\mathrm{PAH}$ ratio and the Chandra-ACIS soft X-ray fluxes for our sources. For the ACIS fluxes we assume a nominal 20% uncertainty, based on Chandra catalogues of point sources such as Servillat et al. (2008).

Nebular line emission

Fine-structure emission lines are an important diagnostic of the physical conditions in star-forming region. Their strengths and ratios constrain physical parameters such as the hardness of the radiation field, gas density, or the presence of shocked gas. In the mid-IR, several forbidden lines are observable from species such as [Ne II], [Ne III], [S III] and [S IV]. In Table 3.6 we list the continuum-subtracted nebular line strengths in NGC 604, as measured with the PAHFIT tool, which performs Gaussian fits to the nebular lines.

We have also measured the continuum-subtracted line strengths in the hires data for targets A, B and C in the right panel of Fig. 3.2. We have fitted Gaussian profiles to the lines, this time using the built-in tool for that purpose included in the SMART software. We show the resulting line strengths in Table 3.7.

Two of the most prominent lines are [S IV]10.5μm and [Ne II]12.8μm. Fig. 3.5 shows continuum-subtracted maps of these two lines, and illustrates the regions from where the line emission originates. At the resolution of the maps there is spatial coincidence between the peaks of line emission and the infrared sources we have identified. Sources of particularly bright line emission are sources 1, 4 and 7. The localized nature of the emission allows investigations of the physical conditions in the individual sources.

3.3.3 Electron density

The ratio of two lines of the same ionization state of a single species, emitted from levels with similar excitation energies, can be used as a tracer of the electron density n_e (Rubin et al. 1994). We use the [S III]18.7μm/[S III]33.6μm to investigate the electron densities in the NGC 604 region, based on the lores line ratios. We use the lores data rather than the

Source	**PAH$_{6.2\mu m}$** 10^{-6} **W m^{-2} sr^{-1}**	**PAH$_{7.7\mu m}$** 10^{-6} **W m^{-2} sr^{-1}**	**PAH$_{8.6\mu m}$** 10^{-6} **W m^{-2} sr^{-1}**	**PAH$_{11.3\mu m}$** 10^{-6} **W m^{-2} sr^{-1}**	**PAH$_{17\mu m}$** 10^{-6} **W m^{-2} sr^{-1}**
Src 1	2.56(0.10)	7.96(0.54)	1.28(0.12)	1.33(0.16)	0.85(0.26)
Src 2	1.76(0.07)	5.49(0.38)	0.87(0.09)	1.07(0.11)	0.73(0.17)
Src 3	1.24(0.07)	2.82(0.33)	0.51(0.09)	0.83(0.14)	1.15(0.24)
Src 4	1.51(0.07)	4.25(0.35)	0.64(0.09)	0.76(0.13)	0.88(0.23)
Src 5	0.93(0.03)	2.42(0.19)	0.50(0.04)	0.52(0.05)	0.24(0.07)
Src 6	0.14(0.01)	0.48(0.03)	0.06(0.01)	0.11(0.01)	0.06(0.03)
Src 7	1.64(0.08)	5.14(0.41)	0.91(0.10)	1.04(0.14)	0.26(0.07)
NGC 604	0.40(0.02)	1.16(0.09)	0.19(0.02)	0.25(0.03)	0.11(0.04)

Table 3.4 PAH feature strengths.

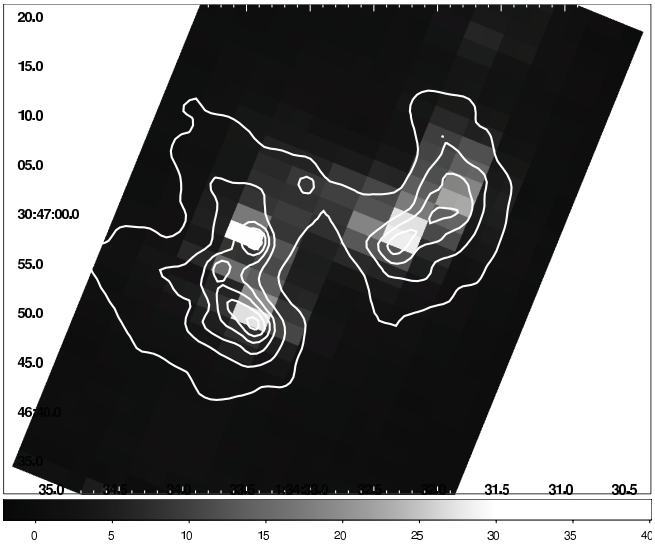

(a)

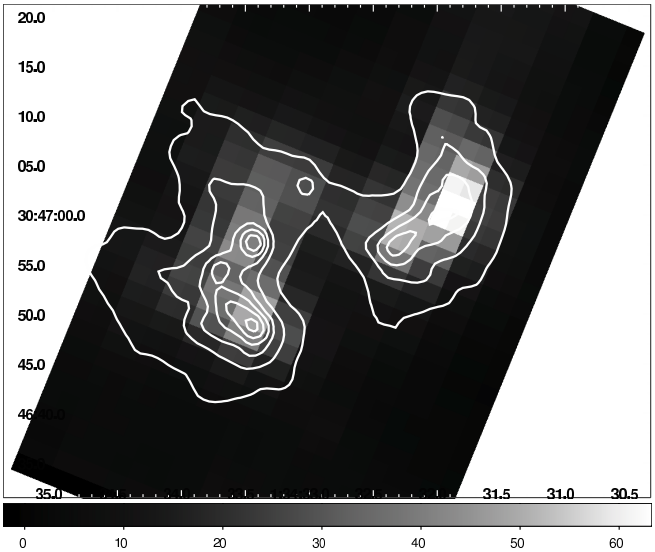

(b)

Figure 3.5 Continuum-subtracted line emission in NGC 604, in units of MJy sr^{-1}. *(a)* [S IV]10.5μm emission has well defined peaks near sources 1, 4 and C. *(b)* [Ne II] peaks near source 7. The white contours are IRAC 8 μm emission.

Source	**PAH$_{17\mu m}$/(ΣPAH)**	$F_{X_{soft}}$ **[10^{-9} erg** cm^{-2} s^{-1}**]**
Src 1	0.065(0.020)	0.84
Src 2	0.079(0.019)	1.37
Src 3	0.213(0.047)	3.70
Src 4	0.123(0.033)	2.50
Src 5	0.055(0.016)	1.64
Src 6	0.076(0.038)	1.65
Src 7	0.030(0.002)	0.91
NGC 604	0.055(0.020)	-

Table 3.5 Ratio of PAH 17 μm to the sum of all other PAH features.

hires data because the two [S III] lines are measured at similar spatial resolutions in the lores data, while for the hires data they are measured in two different apertures ([S III]18.7 falls on the SH module, while [S III]33.6 falls in the LH module).

The [S III]18.7μm/[S III]33.6μm ratios calculated from Table 3.6 are very uniform in the region, varying from 0.51 to 1.02, with the highest value near source 7, in the NW infrared lobe. These values are very close to the low density limit discussed in Dudik et al. (2007) (their Fig. 9), and hence our data provide only upper limits for the electron densities. Using the Dudik et al. (2007) diagram, we derive upper limits for the electron densities between log $n_e = 1.5$ cm^{-3} and log $n_e = 2.5$ cm^{-3} in the region.

3.3.4 Hardness of the radiation field

We investigate the hardness of the radiation field in the region by looking at the line ratio [S IV]10.5μm/[Ne II]12.8μm. The use of these two lines has an observational motivation. The two lines are within the SL wavelength range and hence have the same spatial scale and pixel size, which is not the case for the [Ne III]/[Ne II] ratio. The ionization potential required to produce [Ne II] is only 21.6 eV, while it takes 34.8 eV to ionize [S III] to obtain [S IV]. Hence, the ratio between these two ionic species traces the hardness of the radiation field, which can be interpreted in terms of stellar ages, with [Ne II] tracing star formation activity during the last 10 Myr and [S IV] tracing massive stars born in the last 4-6 Myr. In Fig. 3.6 we show the corresponding line ratio map obtained from the spectral cube. Note that the color scale of the map is in logarithmic units.

The mid-IR line ratios do not only depend on the hardness of the radiation field. They also depend on the ionization state of the gas, that can be parametrized using the ionization parameter Q (the ratio of the ionizing photon density to gas density). In Martínez-Galarza et al. (2011) (MG11 hereafter) we have used the hires line ratios as derived from the measurements done in Lebouteiller et al. (2008), and combined them with the radiative transfer models in Levesque et al. (2010) using the interactive IT-ERA software (Groves & Allen 2010), to break the degeneracy between age and ionization parameter in the particular case of the 30 Doradus region. We found in that

Source	**[Ar II]**6.9μ**m** 10^{-7} **Wm**$^{-2}$**sr**$^{-1}$	**[Ar III]**8.9μ**m** 10^{-7} **Wm**$^{-2}$**sr**$^{-1}$	**[S IV]**10.5μ**m** 10^{-7} **Wm**$^{-2}$**sr**$^{-1}$	**[Ne II]**12.8μ**m** 10^{-7} **Wm**$^{-2}$**sr**$^{-1}$
Src 1	0.58(0.19)	2.05(0.33)	3.07(0.42)	4.61(0.64)
Src 2	0.60(0.17)	0.58(0.16)	0.84(0.14)	2.89(0.40)
Src 3	0.59(0.14)	0.90(0.34)	1.54(0.28)	3.18(0.39)
Src 4	0.48(0.16)	2.05(0.31)	4.02(0.53)	3.39(0.52)
Src 5	0.51(0.08)	0.47(0.09)	0.32(0.06)	1.85(0.19)
Src 6	0.15(0.02)	0.35(0.04)	0.25(0.03)	1.28(0.11)
Src 7	0.93(0.21)	2.59(0.35)	2.68(0.45)	6.80(0.86)
NGC 604	0.17(0.04)	0.29(0.06)	0.34(0.04)	1.04(0.11)
Source	**[Ne III]**15.5μ**m** 10^{-7} **Wm**$^{-2}$**sr**$^{-1}$	**[S III]**18.7μ**m** 10^{-7} **Wm**$^{-2}$**sr**$^{-1}$	**[S III]**33.7μ**m** 10^{-7} **Wm**$^{-2}$**sr**$^{-1}$	**[Si II]**34.8μ**m** 10^{-7} **Wm**$^{-2}$**sr**$^{-1}$
Src 1	4.83(0.67)	6.41(0.91)	6.64(1.13)	2.54(0.76)
Src 2	2.81(0.40)	3.53(0.54)	4.29(0.76)	1.74(0.53)
Src 3	3.84(0.47)	5.66(0.83)	7.90(1.40)	3.29(0.96)
Src 4	4.08(0.48)	5.37(0.79)	6.52(1.13)	2.57(0.76)
Src 5	1.15(0.13)	2.21(0.23)	4.37(0.72)	1.90(0.47)
Src 6	1.02(0.11)	1.65(0.01)	2.34(0.01)	0.90(0.01)
Src 7	7.02(0.94)	9.10(1.30)	8.90(1.11)	3.15(0.74)
NGC 604	1.04(0.10)	1.57(0.01)	1.90(0.01)	0.77(0.01)

Table 3.6 Fine structure line fluxes as extracted from the lores data.

study that the [Ne III]15.5μm/[Ne II]12.8μm and the [S IV]10.5μm/[S III]18.7μm ratios in 30 Doradus are compatible with starburst ages $\leq$ 3.0 Myr and ionization parameters 8.0 cm s^{-1} $\leq$ log Q $\leq$ 8.6 cm s^{-1}.

We perform a similar analysis for NGC 604. In Fig. 3.7 we plot the ratios computed from Table 3.6 as compared to a set of Levesque et al. (2010) models with the sub-solar metallicity of NGC 604 ($Z = 0.4Z_{\odot}$) and low electron density ($n_e = 10$ cm^{-3}), in accordance with the low density regime inferred from the line ratios. The overall line ratios are indicative of an age of between 4 and 4.5 Myr. Differences in age and ionization parameter between the sources can be inferred from the plot. Sources 1 and 4 have larger ionization parameters and older ages, while sources 2,3 and 7 have line ratios consistent with younger ages. The IRS map resolution is not enough to resolve the sources individually, and hence some confusion between the emission line from different sources is expected. Nevertheless, the trend towards younger ages inferred from Fig. 3.7 for the brightest IR sources is a good indication of recent star formation activity in those locations.

Using the hires line fluxes we also measure the strength of the radiation field in sources A, B and C with the parametrization of Beirão et al. (2006), which uses the [Ne III]/[Ne II] to estimate the strength as the product of the field intensity and the field hardness:

Source	**[S IV]**10.5μ**m** $10^{-20}\times$**W cm**$^{-2}$	**[Ne II]**12.8μ**m** $10^{-20}\times$**W cm**$^{-2}$	**[Ne III]**15.5μ**m** $10^{-20}\times$**W cm**$^{-2}$	**[S III]**18.7μ**m** $10^{-20}\times$**W cm**$^{-2}$	**[S III]**33.7μ**m** $10^{-20}\times$**W cm**$^{-2}$	**[Si II]**34.8μ**m** $10^{-20}\times$**W cm**$^{-2}$
Src A	1.63(0.36)	3.71(0.14)	4.24(0.08)	4.54(0.12)	5.54(0.07)	1.85(0.09)
Src B	2.24(0.22)	4.24(0.24)	5.52(0.12)	5.49(0.12)	9.03(0.09)	2.76(0.09)
Src C	2.60(0.46)	5.77(0.24)	6.63(0.02)	7.29(0.18)	10.08(0.09)	2.71(0.11)

Table 3.7 Fine structure line fluxes as extracted from the hires data.

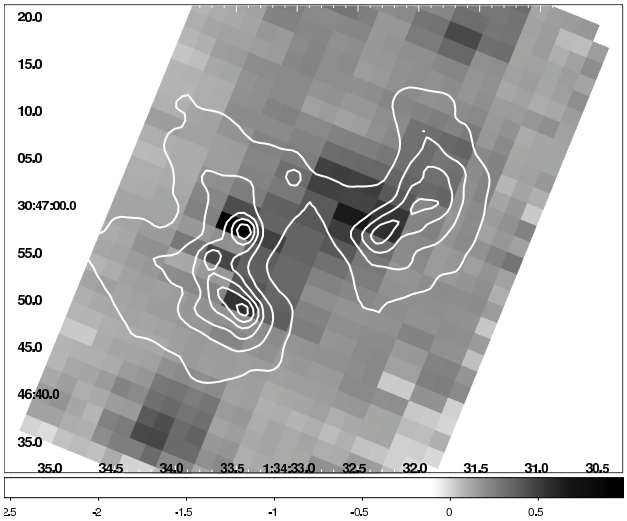

Figure 3.6 The log([S IV]10.5μm/[Ne II]12.8μm) ratio in NGC 604 as derived from the spectral map. For reference, the IRAC 8 μm contours (white) are superimposed. We use the measured ratios to estimate the hardness of the radiation field towards specific locations (see text).

$$\left(F_{[\mathrm{Ne\,II}]12.8\mu\mathrm{m}} + F_{[\mathrm{Ne\,III}]15.6\mu\mathrm{m}}\right) \times \frac{F_{[\mathrm{Ne\,III}]15.6\mu\mathrm{m}}}{F_{[\mathrm{Ne\,II}]12.8\mu\mathrm{m}}} \tag{3.1}$$

We get a radiation field strength of 9.1×10^{-20} W cm^{-2}, 12.7×10^{-20} W cm^{-2} and 14.25×10^{-20} W cm^{-2} for sources A, B and C respectively.

3.3.5 [Si II] emission

Most of the lines listed in Table 3.6 are from regions with ionized hydrogen gas. The exception is [Si II], which originates in a variety of environments including H II regions, but also X-ray dominated regions (Maloney et al. 1996), high density PDRs (Kaufman et al. 2006) and regions of shocked gas, where heavy elements are returned to the gas phase. It is in general hard to pin down the physical mechanism for the emission of [Si II]. We investigate this in NGC 604 by looking at a possible correlation between the ratio [Si II]/[Ne II] and the ratio of PAH emission at 17 μm to all other PAH features together. We plot the relation between these two ratios in Fig. 3.8. In §3.4.2 we discuss this finding in the context of several possible scenarios for the emission of [Si II].

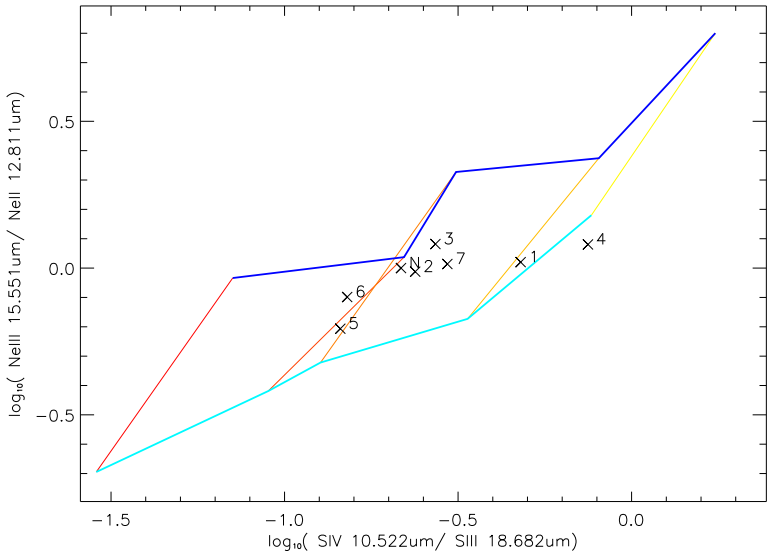

Figure 3.7 Comparison of the line ratios in NGC 604 with the Levesque et al. (2010) models. The [Ne III]15.5μm/[Ne II]12.8μm ratio is plotted versus the [S IV]10.5μm/[S III]18.7μm ratio. Data points from Table 3.6 are overplotted to the grid of models, that cover a range of ages from 4 Myr (blue) to 4.5 Myr (cyan) and a range of ionization parameters from 4×10^7 cm s^{-1} (yellow) to 4×10^8 cm s^{-1} (red). The line ratio for the integrated map is indicated by "N".

3.3.6 H_2 emission

Additional diagnostics on the physical conditions in NGC 604 come from the molecular hydrogen lines arising from pure rotational transitions at 12.27 μm (0-0 S(2)) and 17.03 μm (0-0 S(1)), which we detect (although marginally in the case of the 12.27 μm line) in the hires modules of the IRS in sources A, B and C. Using the same procedure as for the nebular lines, we fit Gaussian profiles to the H_2 rotational lines and estimate their strengths. In Table 3.8 we list the measured line strengths.

H_2 temperatures can be calculated from the ratio of the two detected line strengths listed in Table 3.8, using a general method (see, for example the Appendix of Brandl et al. 2009). This method holds under the following assumptions: *(i)* the gas is in local thermodynamic equilibrium (LTE); *(ii)* the hydrogen rotational lines are optically thin; *(iii)* the critical densities for the lines are $< 10^3$ cm^{-3} and *(iv)* the two states of the H_2 molecule, ortho-H_2 and para-H_2, exist in a ratio of 3 to 1. From the Boltzmann statistics that describe the distribution of energy states for the H_2 molecule and the relation between the line strength and the H_2 column density, it can be shown that the excitation temperature is given by:

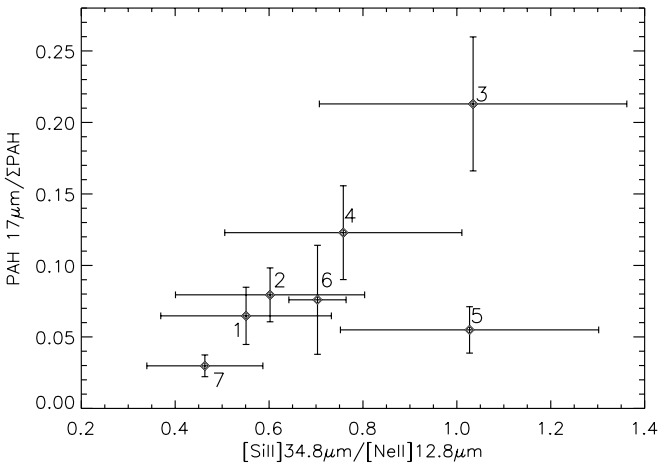

Figure 3.8 The [Si II]/[Ne II] ratio plotted against the ratio of $PAH_{17\mu m}$ strength to the strength of all other PAH features, for our sources. Error bars in both quantities are shown.

Source	**H_2 S(2)12.27μm [$10^{-20}\times$W cm^{-2}]**	**H_2 S(1)17.03μm [$10^{-20}\times$W cm^{-2}]**	T_{ex} **[K]**
Src A	0.19(0.15)	0.20(0.01)	520
Src B	0.13(0.15)	0.13(0.02)	540
Src C	0.16(0.04)	0.14(0.01)	490

Table 3.8 H_2 rotational lines.

$$T_{ex} = \frac{E_2 - E_1}{k \ln\left(C \frac{\lambda_1}{\lambda_2} \frac{F_1}{F_2}\right)} \tag{3.2}$$

where E_1 and E_2 are the energies of the involved levels, k is the Boltzmann constant, C is a constant dependent on the ratio of Einstein coefficients and statistical weights, λ_1 and λ_2 are the rest-frame wavelengths of the observed lines, and F_1 and F_2 their respective integrated line fluxes. We list the computed temperatures in Table 3.8.

3.3.7 SED modeling

In MG11 we have presented a Bayesian fitting tool to study the infrared SEDs of star-forming systems. The tool is based on a grid of the Dopita & Groves models (D&G models hereafter), which are thoroughly described in a series of papers (Dopita et al. 2005, 2006b,c, Groves et al. 2008). Here we briefly describe the tool and then apply it to

the observed infrared SED of NGC 604 in §3.4.2, including both the IRS spectrum and the PACS photometry, to derive statistically meaningful values for the following physical parameters of the region: cluster age and stellar mass, compactness, fraction of total mass contained in embedded objects and fraction of the luminosity arising in photon-dominated regions.

Physics

The D&G models combine stellar synthesis, radiative transfer, dust physics and self-consistent dynamical evolution of individual H II regions to simulate the UV to sub-millimeter spectral energy distributions (SEDs) of star-forming regions, including thermal emission from dust and PAHs, and nebular line emission. Using all the available spectral information, for a given metallicity (Z) and ambient interstellar pressure (P_0/k), the fitting tool computes probability distribution functions (PDFs) for key model parameters such as stellar cluster age ($t_{\rm cl}$), cluster mass ($M_{\rm cl}$), compactness (C), fraction of the total luminosity arising in the PDRs ($f_{\rm PDR}$) and the mass contribution from a component of young embedded objects that we model as Ultra Compact H II Regions ($M_{\rm emb}$).

We have defined these parameters in Chapter 2. Of relevance here is the definition of C. This parameter is proportional to the product $M_{\rm cl}^{3/5}(P_0/k)^{2/5}$, and sets the evolution of dust temperature with time. If L_* is the luminosity of the cluster and $R_{\rm HII}^2$ is the radius of the H II region, then C parametrizes the incident heating flux, $L_*/R_{\rm HII}^2$ and controls the position of the far-IR bump of the SED for a given value of P_0/K. Intuitively, the compactness provides a measure of how close the dust particles are to a stellar heating source of certain luminosity. It is important to realize that, for a given compactness, different physical diameters of the sources are expected, depending on the luminosity of the central cluster. This parameter is thus only weakly related to the physical size of the sources.

Priors

Bayesian inference allows to include any previous evidence on the values of the model parameters in the calculation of the posterior probability distribution (the PDF). Here we use flat, bounded priors for all the model parameters, with boundaries set by observational and theoretical studies of star-forming regions, as discussed in MG11. We assume solar metallicity and adopt a thermal pressure of the surrounding ISM of $P_0/k = 10^5$ K cm^{-3}.

The assumption on ISM pressure is supported by measurements of far-IR line ratios from the ISO satellite on a sample of star-forming galaxies (Malhotra et al. 2001). The metallicity of NGC 604 has been measured to be about half-solar (Magrini et al. 2007). However, our experiments show that only the solar metallicity models in our grid are able to reproduce the observed ratio of PAH strength to continuum emission at 100 μm in NGC 604. The discrepancy is most likely due to the specific PAH template used in the D&G models, which is an empirical template based on observations of starburst galaxies. The choice of metallicity does not only affect the PAH emission strength. At far-IR

wavelengths, the change in dust column and mechanical luminosity of the starburst with metallicity produces a slight shift and a broadening of the far-IR bump. While this implies an additional degeneracy with the compactness parameter, the additional errors introduced in the determination of C are smaller than our chosen step size for the compactness grid, which is 0.5.

χ^2 Weighting

In MG11 we have included a discussion of the observational uncertainties involved in measuring the IRS fluxes, which include absolute and relative flux calibrations and systematic errors due to specific observing conditions. Based on that discussion, for fitting purposes we have adopted a uniform uncertainty of 10% across the IRS wavelengths, which also implies a uniform weighting for all data points in the fitting.

The χ^2 minimization procedure described in MG11 has been slightly modified here to ensure that the χ^2 minimization is not dominated by the IRS range, which has many more resolution elements, as compared to only two data points at 100 μm and 160 μm from PACS. Each bin contributes to the χ^2 with a weight that is proportional to the bin size in the logarithmic wavelength space. The bin size is set by the resolution of the models in the IRS range and by the wavelength separation between data points for the PACS data. This results in a weighting function that increases uniformly in the IRS range so that the bins at the short wavelength end (around 5 μm) have about half the weight of those at 35 μm and about 0.25 times the weight of the PACS bins. In section §3.4.2 we apply this tool to the observed SED of NGC 604.

Color correction of PACS photometry

The D&G models compute the monochromatic flux densities for each wavelength bin. However, the flux densities measured by the PACS filters at 100 μm and 160 μm are not monochromatic. They are the integrated flux densities over certain wavelength ranges, as modulated by the filter response function. Before we compare the model fluxes to the observed PACS photometry, it is necessary to evaluate the errors introduced by this difference. To do so, we adopt the method described in da Cunha et al. (2008) to predict the flux density of a source when observed using a given filter. According to their approach, the flux density for any filter is:

$$\mathrm{F}_{\nu}^{\lambda_0} = \frac{\lambda_0^2}{\mathrm{c}} \mathrm{C}_{\nu_0} \frac{\int \mathrm{d}\lambda\, \mathrm{F}_{\lambda}\, \lambda \mathrm{R}_{\lambda}}{\int \mathrm{d}\lambda\, \mathrm{C}_{\lambda}\, \lambda\, \mathrm{R}_{\lambda}} \tag{3.3}$$

where

$$\lambda_0 = \frac{\int \mathrm{d}\lambda\, \lambda\, \mathrm{R}_{\lambda}}{\int \mathrm{d}\lambda\, \mathrm{R}_{\lambda}} \tag{3.4}$$

is the effective wavelength of the filter response R_λ, c is the speed of light and C_λ is a calibration spectrum that depends on the photometric system used for the calibration. In

the case of the PACS photometer, the calibration spectrum is constant ($C_\lambda \lambda$ = constant), which simplifies the calculations. Using this method, and the filter response curves available at the Herschel Science Center, we have computed effective wavelengths for the PACS filters at $L_0^{100} = 102.6\,\mu$m and $L_0^{160} = 167.2\,\mu$m, and we estimate that the difference between the monochromatic and filter fluxes in the models are < 1% for the PACS green filter (100 μm) and ~ 9% for the PACS red filter (160 μm). These uncertainties are within the 10% observational errors.

3.4 Discussion

3.4.1 Notable sources

The most striking morphological characteristic of the sources labelled 1-7 in Fig. 3.2 is that most of them (sources 1-5) are well defined, individual infrared-bright knots. Sources 1, 2, 7 and 4 are, in that order, the strongest sites of PAH emission, as shown in Table 3.4. They are also associated with less steep continuum slopes, as shown in Table 3.3. This implies a component of emission from warm (300 K) dust that peaks at about 15 μm, in the vicinity of sources with strong 8 μm emission. These regions are the locations where most of the MYSO candidates have been identified by Fariña et al. (2012) using NIR photometry.

Source 2

This source, located in the SE lobe, is bright in all IRAC bands but has no optical, Hα or FUV counterpart. In addition, it has one of the strongest silicate absorptions at 10 μm as shown in Fig. 3.3, and it is very close to the peak of one of the CO clouds reported in Wilson & Scoville (1992). Using HST data, Maíz-Apellániz et al. (2004) derived an extinction map for the region. They found a strong peak of extinction at the location of source 2, which is consistent with its relatively strong silicate absorption. Compared with all the other sources, nebular emission towards this source is weak (Table 3.6). Its high optical extinction, bright PAH emission and spatial coincidence with a reservoir of molecular gas makes of source 2 a very good candidate for a site of embedded star formation.

Source 5

From the $F_{15\mu m}/F_{30\mu m}$ ratios listed in Table 3.3, we infer that Source 5 has the coldest dust temperature among our sources. Its [S IV]10.4/[S III]18.7 and [Ne III]15.5/[Ne II]12.8 line ratios derived from Table 3.6 are both the lowest among our sources and the PAH features listed in Table 3.4 are weaker towards this source, compared with all the other well defined IR knots. The combination of cold dust, low ionization state, soft radiation field (as traced by the line ratios), and weak emission from PDRs are indicative of a more evolved stage

for this particular source. In fact, source 5 is located near the boundary between the active star-forming western and quiescent and older eastern hemisphere of NGC 604, as catalogued by Tüllmann et al. (2008). Source 5 is also brighter than all the other sources at 3.6 μm. This band traces the 3.3 μm PAH feature, very hot dust and photospheric emission from stellar populations older than 10 Myr, but since the continuum slope is not indicative of hot dust and the PAH emission is weak towards this source, the most plausible explanation for the excess at 3.6 μm is the presence of stars older than 10 Myr.

Source 7, Source 4 and Source 1

Source 7, located in the NW infrared lobe, shows the strongest nebular line emission among our sources (Table 3.6). This source is very close to a bright ridge of photospheric optical emission from a nearby group of young stars (see Fig. 3.2). The higher electron density near the NW lobe is consistent with the strong nebular lines measured near source 7 and with the enhanced Hα emission observed in this same area of NGC 604 (see, for example, Fig. 2 in Relaño & Kennicutt (2009)), and implies a higher ionization state. This source is most likely the location of the youngest main sequence stars of the cluster. This is supported by our measurements of the radiation field strength in the neighbouring source C, where we have measured a stronger radiation field using Eq. 3.1, relative to the other sources.

The [S IV]/[Ne II] ratio map of Fig. 3.6 peaks at source 4, which has a relatively weaker radiation field. This suggests an enhanced radiation filed hardness near this location, where we have also measured a warm dust component from the spectral continuum slope (Table 3.3). Another location with relatively hard radiation field is source 1. The Relaño & Kennicutt (2009) study of the region reveals enhanced Hα emission in sources 1, 4 and 7. However, the eastern part of NGC 604, where sources 1 and 4 are located, has a higher optical extinction traced by the Balmer optical thickness ($\tau_{\rm Bal} \sim 1.2$), as compared with the surrounding average extinction ($\tau_{\rm Bal} = 0.2 - 0.3$) (Maíz-Apellániz et al. 2004). The [S IV]10.5μm falls on the broad silicate absorption feature near 10 μm, and this leads to an underestimation of the [S IV]/[Ne II] ratio in regions of high extinction. Although this does not affect our general picture about the radiation hardness, larger [S IV]/[Ne II] ratios and hence younger ages might be expected in sources 1 and 4 from extinction corrected [S IV]/[Ne II] ratios.

Finally, the [S IV]10.5μm/[Ne II]12.8μm ratio is sensitive not only to the cluster age, but also to the gas density. However, at the relatively low electron densities measured in the region ($\log n_e \approx 1.5 - 2.5$ cm^{-3}), we do not expect the measured line ratios to be significantly affected.

3.4.2 The evolutionary stage of NGC 604

Fig. 3.9 shows the best fit to the observed integrated SED of NGC 604 (IRS + PACS) using the Bayesian tool described in §3.3.7. Also, in Fig. 3.10 we show the resulting PDFs, covering the totality of our parameter space, and in Table 3.9 we list the associated best

Parameter	Best fit value	Eldridge & Relaño (2011)
$t_{\rm cl}$ (Myr)	$4.0^{+1.0}_{-1.0}$	> 4
$\log C$	$5.5^{+0.5}_{-0.5}$	
$f_{\rm PDR}$	$0.5^{+0.3}_{-0.2}$	
$M_{\rm cl}$ (10^5 M$_\odot$)	$1.6^{+1.6}_{-1.0}$	$(3.8 \pm 0.6) \times 10^5$
$M_{\rm emb}$ (10^4 M$_\odot$)	$1.2^{+1.3}_{-0.1}$	
$f_{\rm emb}$	0.075	

Table 3.9 Best fit to the integrated spectrum of NGC 604. Parameters listed are, from the top: the cluster age, the compactness, the fraction of total luminosity arising in PDR regions, the stellar mass of the cluster, the mass contained in embedded objects, and the ratio of embedded to stellar mass.

fit parameters and uncertainties, with the values for $t_{\rm cl}$ and $M_{\rm cl}$ determined independently by Eldridge & Relaño (2011) using several methods, including optical SED fitting. We also include $f_{\rm emb}$, the ratio of mass contained in young embedded objects ($M_{\rm emb}$) to stellar mass in the cluster ($M_{\rm cl}$). This Bayesian fit, as well as the other spectral features discussed above, provide a wealth of information about the physics and the evolutionary stage of NGC 604.

A remarkable fact is highlighted by a comparison between the PDFs shown in Fig. 3.10 and those obtained for 30 Doradus and shown in in Fig. 2.7. The distribution of probability over the parameter space considerable shrinks in the case of NGC 604. In particular, the PDFs of Fig. 3.10 do not show the bi-modal degeneracies that are evident in Fig. 2.7. The improvement is related to the inclusion of the *Herschel* data in the analysis. Far-infrared observations greatly help constraining model parameters such as the compactness, thus breaking this degeneracy. Nevertheless, as we have seen in Chapter 2, in the degenerate case the Bayesian tool chooses the solution that better represents the conditions in a regio, using the information from the nebular lines. Therefore, although data at longer wavelengths further constrain the model parameters, the best fit parameter obtained using mid-IR data only remain practically unchanged.

Dust temperature and compactness

The thermal continuum, PAH emission and line emission are well reproduced by the best fit. The combined IRS and PACS data are consistent with a far-IR SED peaking at approximately 70 μm, which indicates an effective dust temperature of $\sim$ 40 K. Using multi-wavelength photometry of a sample of H II regions in the Magellanic Clouds, Lawton et al. (2010) show that the infrared SEDs of most of these regions peak at 70 μm. Our result indicates that this average dust temperature is not unique of "local" H II regions, but also applies to at least one relatively more distant region.

We have stated that the compactness parameter controls the incident heating flux

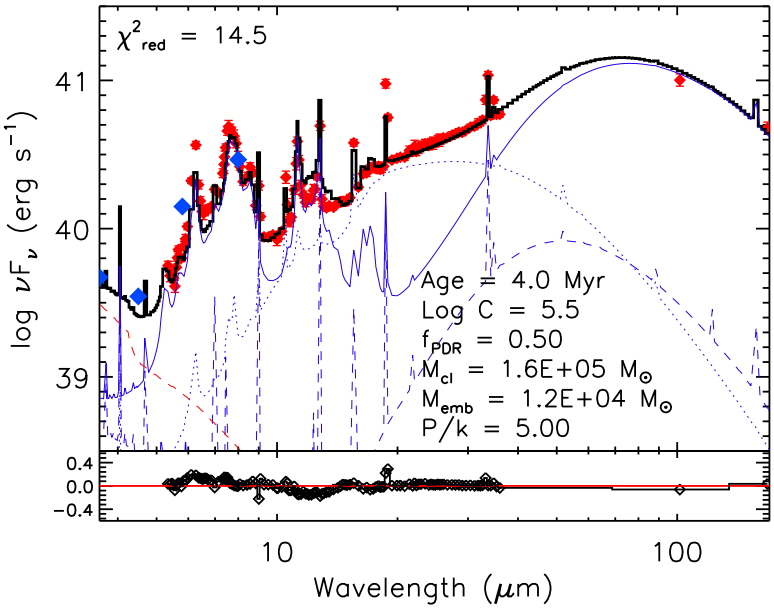

Figure 3.9 Best fit model to the integrated SED of NGC 604. The IRS and PACS data are shown as red diamonds, and the IRAC photometry as blue diamonds. The solid line is the best fit model. Also shown are the contributions from pure H II region emission (dashed blue), PDR (solid blue), embedded population (dotted blue) and photospheric emission from stars older than 10 Myr (dashed red). Residuals are shown in the bottom panel.

$L_*/R_{\rm HII}$ as a function of age of the H II region. From our given set of best fit parameters it is then possible to derive an incident heating flux (see Fig. 3 in Groves et al. 2008). We obtain an incident flux of $\log(L_*/R_{\rm HII}) = 0.65$ erg s^{-1} cm^{-2} for our best fit values of compactness and age. The bolometric luminosity of the cluster can be obtained from integration of the best fit SED, and gives approximately 6.0×10^{41} erg s^{-1}, which allows us to solve for the effective radius of the H II region. We obtain $R_{\rm HII} \sim 120$ pc. This value corresponds to the scale of the larger filaments observed in NGC 604 (Fig. 3.2). This agreement between a model-derived quantity and a measurable observable demonstrates the capabilities of our Bayesian approach to obtain valuable physical information when applied to unresolved star forming regions.

Stellar mass

The total stellar mass of $1.6^{+1.6}_{-1.0} \times 10^5$ $M_\odot$ that we estimate with the SED fitting is in agreement with the value derived by Eldridge & Relaño (2011) and indicates a total stellar mass similar to that of the 30 Doradus region, for which we find a total stellar mass of

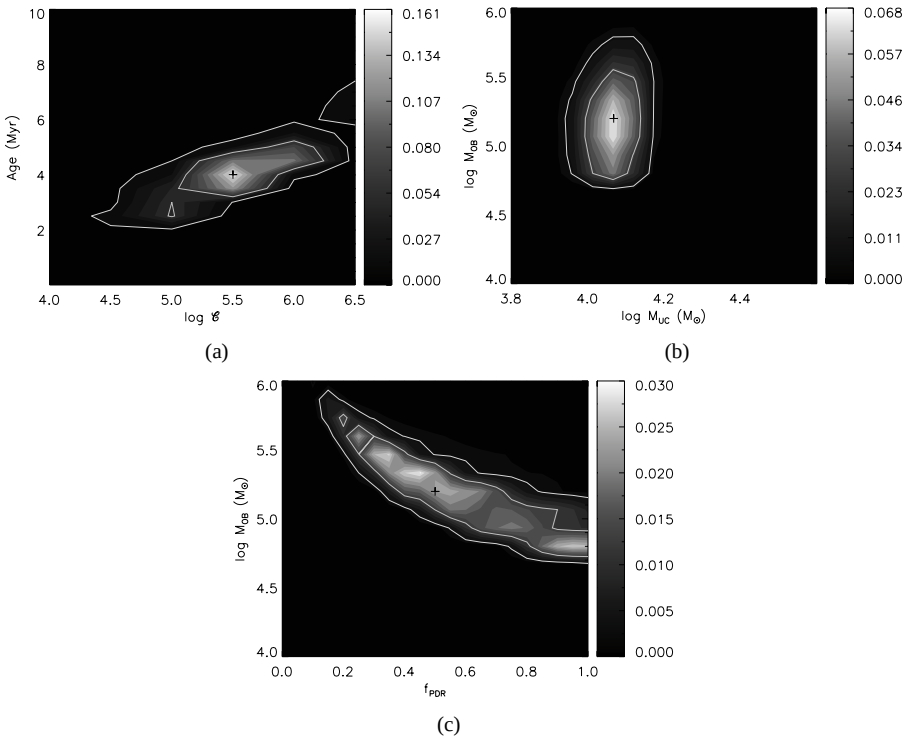

Figure 3.10 Two-dimensional PDFs for selected pairs of parameters covering the totality of the parameter space. The pairs shown are: *(a)* $\log C$ - $t_{\rm cl}$, *(b)* $\log \mathrm{M_{emb}}$ - $\log \mathrm{M_{cl}}$ and *(c)* $f_{\rm PDR}$ - $\log \mathrm{M_{cl}}$. The grey scale contours indicates the normalized probability. The cross symbols mark the best-fit values while the white contour lines indicate the 1-σ and 90% confidence levels.

$0.63^{+0.37}_{-0.23} \times 10^5\,\mathrm{M}_\odot$ in MG11. In general, the total stellar mass in 30 Doradus is larger than in NGC 604. Our result indicates a slightly lower mass for 30 Doradus which may be due to the fact that the physical projected area covered in our 30 Doradus map is smaller than the projected area of the map presented in this chapter.

We observe in Fig. 3.10(c) the same degeneracy between cluster mass and fraction of the total luminosity from PDRs that we found for 30 Doradus in Chapter 2. We have argued that the reason for this degeneracy is the fact that both the the PDR and the pure H II region spectra contribute to the dust thermal continuum. An increase in PAH from emission is accompanied by an increase in the overall infrared luminosity. This also renders the additional far-infrared data insufficient to solve this degeneracy. At optical wavelengths, where the emission from PDR is significantly different from that of an H II region, are needed to settle the issue. Nevertheless, the degeneracy between $M_{\rm cl}$ and $f_{\rm PDR}$ implies that the the Bayesian fitting tool based on the D&G models can find solutions that

fit both the optical and infrared mass estimates found by Eldridge & Relaño (2011) and Relaño & Kennicutt (2009) respectively.

Age of the region

The fraction of total mass contained in embedded objects measured here for NGC 604 ($f_{\rm emb} \sim 0.08$) is smaller than that measured for 30 Doradus in MG11 ($f_{\rm emb} \sim 0.53$). This is a clear suggestion of an evolutionary difference between these two regions, and points towards 30 Doradus being younger that NGC 604.

Additionally, the age of $\sim 4-5$ Myr derived with our fitting method is consistent with the study of the line ratios that we presented in §3.3.4 and agrees well with the studies by Eldridge & Relaño (2011) and Hunter et al. (1996). Statistically, and assuming that the majority of the stars in NGC 604 were born in a single star formation event, our result also supports the generally accepted view that NGC 604 is a more evolved star-forming region than its more luminous counterpart 30 Doradus, for which we have derived an age of ~ 3 Myr using the same method in MG11.

PDR content

Although the fraction of total luminosity arising in PDRs is degenerate with the total cluster mass, as shown in Fig. 3.10, our result from SED fitting suggests that at least half of the energy output from NGC 604 is generated in PDRs, the other half arising in ionized regions closer to the cluster stars. The presence of a luminous PDR in NGC 604 is consistent with the findings of Heiner et al. (2009), who find considerably high amounts of atomic hydrogen ($N_{\rm HI} \sim 2.0 \times 10^{21}$ cm^{-2}), and associate them with the photodissociation of H_2 in a dense ($n \sim 500$ cm^{-3}) PDR.

Molecular hydrogen in NGC 604

The H_2 temperatures calculated using Eq. 3.2 and the measured strengths for sources A, B and C are all close to 500 K. Due to the large uncertainties in the H_2 line fluxes we do not study in detail the temperature variations. We only take these values as indicative of the average temperature of the warm gas. For a given value of the molecule angular momentum, the total number of hydrogen molecules is proportional to the strength of the line. Our results on the H_2 S(1) line, which has smaller error bars (Table 3.8), indicate that warm molecular hydrogen is more abundant towards source A, which has the strongest H_2 lines. Source A is near to the peak of CO emission reported in Wilson & Scoville (1992).

Despite some disagreements on the specific conversion factor that should be used, it is generally assumed that CO is a good tracer of cold molecular hydrogen. Our results hence support the co-existence of a warm and a cold phase of molecular hydrogen near source A. The warm component is usually associated with regions heated by interstellar shock waves (Gautier et al. 1976). These regions emit a rich spectrum of rovibrational

and pure rotational H_2 emission. Although these emissions are only marginally detected in the present work, the improved sensitivity of the Mid-Infrared Instrument (MIRI) for JWST will allow a better estimation of the amount of shocked gas in star-forming regions.

Selective destruction of small PAHs

The 17 μm PAH feature is generally associated with out-of-band bending modes of large PAH molecules, containing $\approx$ 2000 C-atoms (Van Kerckhoven et al. 2000). Table 3.5 shows that the relative strength of this feature scales with the X-ray flux. If we adopt the PAH size argument, this implies that it is the ratio of large to small PAH molecules that scales with the X-ray field. In fact, Fig. 3.11 shows that source 3, which shows the largest enhancement of the 17 μm PAH feature among our sources, coincides with a peak of soft X-ray emission. Soft X-ray emission from massive stars can be associated with shocked stellar winds or magnetically confined gas near the wind base, near the stellar coronae (Cassinelli & Swank 1983).

The dissociation of PAH molecules by X-rays has been discussed in Micelotta et al. (2010). They argue that not all X-ray photon absorptions by PAH molecules lead to photodissociation and estimate that after a second electron has been ejected by the PAH molecule via the Auger effect, the molecule is left with an internal energy of 14-35 eV, enough to dissociate small (50 C-atoms) PAHs, but possibly insufficient to dissociate larger molecules. They leave the question of large PAH survival open. Our observations suggest that, at least in the particular case of source 3, X-ray emission from massive stars may be responsible for the dissociation of small PAH molecules, creating an enhancement of the 17 μm feature.

The origin of the [Si II] emission

Fig. 3.8 is suggestive of a correlation between the enhancement of [Si II] and the enhancement of 17 μm PAH emission at scales of tens of parsecs. Despite the relatively large uncertainties in both the PAH ratio and the [Si II]/[Ne II] ratio, the figure indicates clearly that the enhancement of the PAH 17 μm feature scales with the relative strength of the [Si II] emission, with the exception of source 5, which lies outside this correlation. This result suggests a common underlying physical mechanism for the enhancement of both features. We have shown in Table 3.5 that the regions of strongest 17 μm PAH emission also correspond to regions of enhanced X-ray emission. Based on the triple correlation between $\mathrm{PAH}_{17\mu\mathrm{m}}$ emission, [Si II] emission, and soft X-ray flux, we argue that absorption of ambient X-rays may be linked to both the destruction of small PAH molecules and the excitation of [Si II], and produces the correlation observed in Fig. 3.8

As we have pointed out, source 5 is an outlier of this correlation: it shows a relatively large [Si II]/[Ne II] ratio, but very moderate $\mathrm{PAH}_{17\mu\mathrm{m}}/\Sigma PAH$ ratio. It also lies in a region of low X-ray flux, near the edge between the western, active star-forming hemisphere of NGC 604 and the quiescent eastern region where most of the Wolf-Rayet stars are located (Drissen et al. 2008). In this part of NGC 604, the X-ray luminosity is most likely

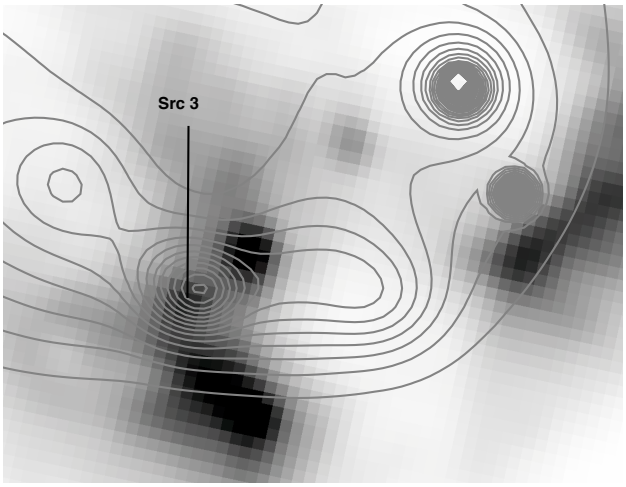

Figure 3.11 Soft X-ray emission in NGC 604. The black and white image is the IRAC 8 μm emission. The line contours correspond to the ACIS image. Source 3 coincides with a local peak of X-ray emission, with a flux of 3.7×10^{-9} erg cm^{-2} s^{-1}.

powered by the SNe activity of an older event of star formation Tüllmann et al. (2008). Based on these facts, we speculate that the [Si II]/[Ne II] ratio for this source is enhanced due to the presence of shocked gas rather than X-ray induced. Although no supernova remnants (SNRs) have been identified in the eastern hemisphere, this is not surprising, since such objects expanding into a low-density gas are hard to detect (Chu & Mac Low 1990).

3.4.3 Ongoing and triggered star formation in NGC 604

Until now, a clear-cut answer on whether or not there is ongoing massive star formation in NGC 604 has been lacking. Although there has been suggestive evidence of embedded star formation in NGC 604 (Fariña et al. 2012, Relaño & Kennicutt 2009) from IR excess studies, a reliable measure of its contribution to the total cluster mass has not been obtained.

In §3.4.1 we have discussed the IR-bright subcondensations that we detect in the IRAC maps. At the distance of NGC 604 it is unlikely that they are individual massive young stellar objects. A fit to their SEDs (shown in Fig. 3.3) using for example the D&G models, reveals that they are consistent with stellar masses between 10^3 M$_\odot$ and 10^4 M$_\odot$, given the uncertainty in the determination of the stellar mass shown in Fig. 3.10(b). This implies that all together they account for at least a few percent of the stellar mass in NGC 604. We have pointed out that the line ratios measured towards some of those clumps, namely sources 2, 3 and 7, are consistent with younger ages than the rest of the sources. Although

the timescales for the dissipation of dusty envelopes around star-forming clusters can be as long as 10 Myr in regions of high density, the low electron density that we have inferred in §3.3.3 implies that NGC 604 is a rather diffuse region. Consequently, we do not believe that sources 2, 3 and 7 are evolved clusters. The presence of these young, massive, IR-bright clusters, some of which have deep silicate absorption features, is a clear indication of significant massive star formation currently taking place in NGC 604.

Additional evidence that supports this scenario comes from our SED fitting analysis. We have shown in Fig. 3.9 and Table 3.9 that a warm ($T \sim 300$ K) component of dust arising in MYSO (that in the D&G frame we model as Ultra Compact H II Regions) is necessary to reproduce the observed SED of NGC 604 at mid-IR wavelengths. As we have pointed out, the required fraction of mass in embedded objects is considerably smaller that that derived for 30 Doradus in MG11, and comparable to the individual sum up of the cluster masses.

In an evolutionary context, sequential star formation in NGC 604 is a plausible scenario to explain our observations. This idea has been explored by other authors before. Based on submillimeter observations of the CO ($J = 3-2$)/CO ($J = 1-0$) ratio, Tosaki et al. (2007) report the existence of a dense ridge of molecular gas that surrounds the main cluster in NGC 604 and extends in the SE-NW direction, closely following the location of our bright IR lobes. To explain their results, they adopt an scenario in which the compression of molecular gas by the mechanical input from the main cluster (the first generation of stars) has triggered a second generation of stars near the NW infrared lobe. The strong radiation field that we observe close to sources C and 7, where main sequence stars are clearly observed, supports the existence of this second generation of highly ionizing stars. Furthermore, the results discussed in this subsection indicate that massive star formation is currently taking place within the SE lobe of NGC 604, even further away from the main cluster, where we have identified the IR-bright subcondensations of Fig. 3.2, some of which are heavily enshrouded by dust (e.g., source 2). This suggests the existence of a third generation of stars forming in the region, the last chapter in a sequential star formation process that started ~ 4 Myr ago.

3.5 Conclusions

We have investigated the physical conditions and quantified the amount of ongoing massive star formation in the star forming region NGC 604. We used a combination of observational and modeling tools, including infrared spectrophotometry and Bayesian SED fitting of Spitzer and Herschel data. Here are our main findings:

1. We have identified several individual bright infrared sources along the luminous PDRs that surround the ionized gas in NGC 604. These sources are about 15 pc in diameter and have luminosity weighted masses between 10^3 $M_\odot$ and 10^4 $M_\odot$.

2. The deep 10 μm silicate absorption feature, mid-IR continuum slope and atomic line ratios towards some of these sources indicate that they are young embedded systems, and most likely the sites of ongoing massive star formation in NGC 604.

Some of them (i.e. source 2) are also associated with gas reservoirs as traced by CO maps. This is in agreement with previous studies that found evidence of embedded star formation in the region.

3. This massive star formation scenario is supported by Bayesian fitting of the integrated spectrum (lines+continuum) of NGC 604 constructed from *Spitzer*-IRS and *Herschel*-PACS observations. Our results indicate that embedded star formation can account for up to 8% of the total stellar mass in NGC 604.

4. The spectral fitting also implies an age of 4.0 ± 1.0 Myr for the region, a total stellar mass of $\sim 1.6 \times 10^5$ $M_\odot$ and an average dust temperature of ~ 40 K. These results are in agreement with independent measurements of these quantities using optical broad band photometry.

5. We measure a stronger than average radiation field near our sources 7 and C. This result is consistent with the sequential star formation scenario adopted in Tosaki et al. (2007), in which a second generation of main sequence stars has formed near this sources, triggered by the mechanical input from the first generation, 4 Myr old main cluster.

6. We find a positive correlation between the strength of the 17 μm PAH feature, the enhancement of the [Si II]/[Ne II] emission and the strength of the X-ray field towards our sources. We propose that X-rays are responsible for both the excitation of [Si II] and the enhancement of the 17 μm feature via selective destruction of large PAH molecules.

7. Our detection of molecular hydrogen in the region indicates gas excitation temperatures of ~ 500 K in NGC 604, and a slightly larger abundance of H_2 near source A, which correlates well with the location of a bright CO cloud reported in Wilson & Scoville (1992).

8. The physical parameters derived for NGC 604, such as its age and fraction of total mass contained in embedded objects indicate that this region is a more evolved H II region, as compared to its its larger sibling 30 Doradus, that we have studied in MG11 using the same Bayesian method employed here. Nevertheless, star formation in NGC 604 is still ongoing, triggered by the earlier bursts.

Acknowledgements

The authors want to thank Médéric Boquien and the HERM33ES team for kindly providing the PACS photometry of NGC 604. This chapter would not have been possible without the hospitality of all the astronomical community at the Lowell Observatory.